Pure Appl. Chem., Vol. 80, No. 11, pp. 2283–2295, 2008.
doi:10.1351/pac200880112283

Nanostructured anode materials for Li-ion batteries*

Nahong Zhao[1], Lijun Fu[1], Lichun Yang[1], Tao Zhang[1], Gaojun Wang[1], Yuping Wu[1,‡], and Teunis van Ree[2]

[1]Department of Chemistry and Shanghai Key Laboratory of Molecular Catalysis and Innovative Materials, Fudan University, Shanghai 200433, China; [2]Department of Chemistry, University of Venda, Thohoyandou 0950, South Africa

Abstract: This paper focuses on the latest progress in the preparation of a series of nanostructured anode materials in our laboratory and their electrochemical properties for Li-ion batteries. These anode materials include core-shell structured Si nanocomposites, TiO_2 nanocomposites, novel MoO_2 anode material, and carbon nanotube (CNT)-coated SnO_2 nanowires (NWs). The substantial advantages of these nanostructured anodes provide greatly improved electrochemical performance including high capacity, better cycling behavior, and rate capability.

Keywords: nanostructured; anode; Li-ion batteries; electrochemical properties; Si; TiO_2; MoO_2; SnO_2.

INTRODUCTION

Nanostructured materials represent a rapidly growing area in the field of Li-ion batteries because of their substantial advantages in terms of mass transport. Transport in nanoparticle systems typically encompasses shorter transport lengths for both electrons and Li^+ ions, higher electrode–electrolyte contact area, better accommodation of the strain of Li^+ insertion/extraction, and in some cases also local anomalies [1–4]. Therefore, elaborate nanocomposites generally show higher reversible capacity [5,6] and better cycling behavior [7] than their simpler antecedents. The large surface/volume ratio and the congruence of the carrier screening length make nanocomposites efficient electrode materials for powerful electrochemical energy storage devices with both high energy density and high power density, due to the pronounced size effects [1], dimensional confinement, and the reduction of the Li^+ diffusion length. Of such nanomaterials, Si-based nanocomposites [8], nanostructured TiO_2 [9], and SnO_2 nanomaterials [7] have received a great deal of attention, and are considered as alternative anode materials.

In this paper, we review the recent progress in advanced nanostructured composites in our laboratory based on core-shell structured Si nanocomposites [10,11], TiO_2 nanocomposites [12,13], a novel MoO_2 anode material [14], and carbon nanotube (CNT)-coated SnO_2 nanowires (NWs) [15], including a short introduction on the latest development of other reported nanomaterials.

*Paper based on a presentation at the 3rd International Symposium on Novel Materials and Their Synthesis (NMS-III) and the 17th International Symposium on Fine Chemistry and Functional Polymers (FCFP-XVII), 17–21 October 2007, Shanghai, China. Other presentations are published in this issue, pp. 2231–2563.

‡Corresponding author: Tel./Fax: +86-21-5566 4223; E-mail: wuyp@fudan.edu.cn

CORE-SHELL STRUCTURED Si NANOCOMPOSITES

Recently, owing to the rapid advancement of electronic technologies, it has become necessary to improve the capacity and cyclability of batteries. Si is regarded as one of the most promising candidates as anode material for Li-ion batteries. Its theoretical capacity (4200 mAh g^{-1}) is much higher than that of commercially available graphite (372 mAh g^{-1}) [16]. However, the cycling performance of Si is poor, owing to the severe volume expansion and shrinkage during Li^+ intercalation and de-intercalation, which results in pulverization of Si particles and eventual loss of Li^+ storage ability [17]. To solve this problem, nanosized Si particles have been utilized and have achieved partial improvement by reducing the absolute volume change. However, a new problem arose for nanosized Si particles due to aggregation during Li^+ insertion/extraction, with resulting formation of larger particles. The nanocharacteristics disappear with an attendant loss of capacity [18]. In some reports, soft matrixes for Si such as C [19], TiN and TiB_2 [20,21], and Ag [22] were introduced to form composites with Si. However, the Si is still not stable and will separate from the soft matrixes, leading to poor cycling. Consequently, improvement is necessary.

Core-shell structured Si/C composites

In a recent report [10], an effective method was used to synthesize a nanosized C-coated Si composite as anode material for Li-ion batteries. Polyacrylonitrile (PAN)-coated Si nanoparticles are formed by emulsion polymerization, and the PAN-coated precursor is heat-treated under argon to generate a Si/C core-shell nanocomposite (Fig. 1a). The conductive carbon shell envelops the Si nanoparticles and suppresses the aggregation of the Si nanoparticles during electrochemical cycling, subsequently ameliorating the capacity retention of this composite anode material (Fig. 1b).

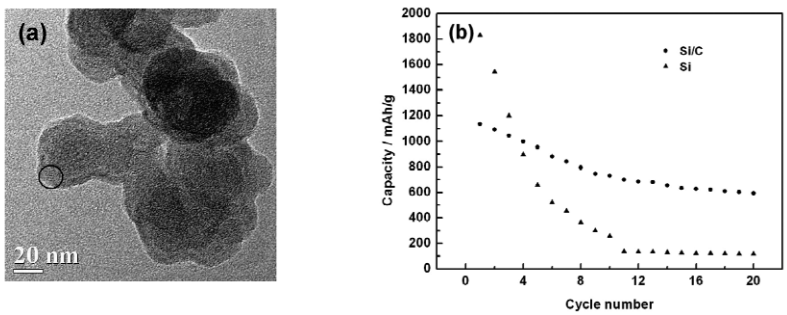

Fig. 1 (a) TEM image of core-shell Si/C nanocomposite and (b) the cycling behavior of the core-shell Si/C nanocomposite.

Meanwhile, the carbon shell combines closely with the nanocores, and significantly enhances the kinetics of Li intercalation and de-intercalation, as well as the apparent diffusion coefficient. The results from cyclic voltammogram (CV) data at different scan rates (Fig. 2a) show that the oxidation peak current at different scan rates was proportional to the root of the scan rate, $v^{1/2}$ (Fig. 2b), indicating that the reaction kinetics was controlled by the diffusion step. Based on the CV data at different scan rates and the following equation [23]:

$$I_p = 2.69 \times 10^5 A n^{3/2} C_0 D^{1/2} v^{1/2} \quad (1)$$

the calculated apparent diffusion coefficient for the Si/C composite was 9.68×10^{-13} cm^2/s, much higher than that of pure Si nanoparticles (1.09×10^{-13} cm^2/s) [22], indicating that the carbon shell at the surface of Si nanoparticles is beneficial for the diffusion of Li^+ since it improves the conductivity

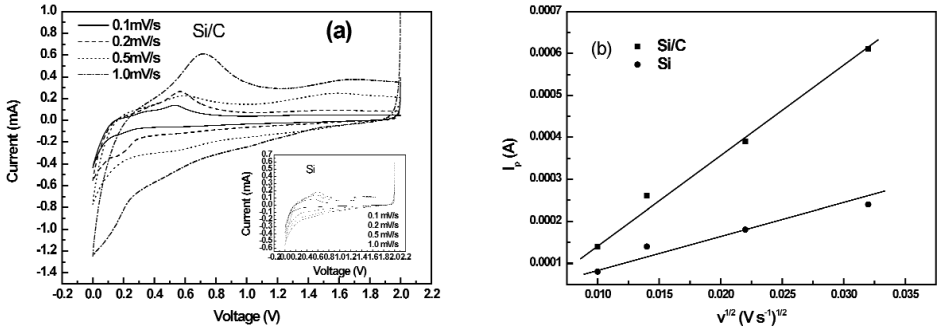

Fig. 2 (a) CVs of the Si/C composite and the virginal Si nanoparticle electrodes (inserted) measured between 0 and 2.0 V vs. Li^+/Li at the scan rates of 0.1, 0.2, 0.5, and 1 mV/s, respectively; (b) relationship between I_p and $v^{1/2}$ of the core-shell Si/C nanocomposite and the virginal Si nanoparticles.

of the composite. It shows that carbon coating is an effective method to improve electrochemical performance of nanosilicon materials.

Core-shell structured Si/SiO composites

We recently synthesized a Si/SiO nanocomposite by a sol-gel method in combination with a subsequent heat-treatment process [11]. At first, molten Si with high purity was irradiated by laser and gasified under an Ar atmosphere, and the condensed Si nanoparticles were collected on a water-cooled wall. Then, the obtained Si nanoparticles were dipped into a stirred tetraethyl orthosilicate (TEOS) sol, followed by the processes of pH adjustment, aging, drying, and heat treatment. Finally, a core-shell structured Si/SiO nanocomposite was synthesized.

Because the Si-hydroxyl groups in the TEOS sol possess high activity, the silica gel can be easily adsorbed onto the surface of the Si nanoparticles. The as-synthesized Si/SiO composites yield a core-shell structure (Fig. 3). Besides, the crystalline structure of the obtained SiO shell is highly compatible with that of nanosilicon, with a face-centered cubic (fcc) structure, which can be seen from the X-ray diffraction (XRD) patterns in Fig. 4.

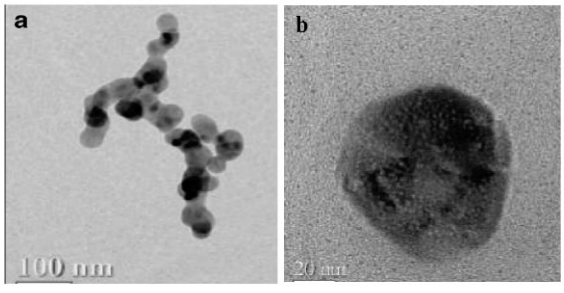

Fig. 3 TEM images of (a) the virginal Si nanoparticles and (b) the Si/SiO nanocomposite.

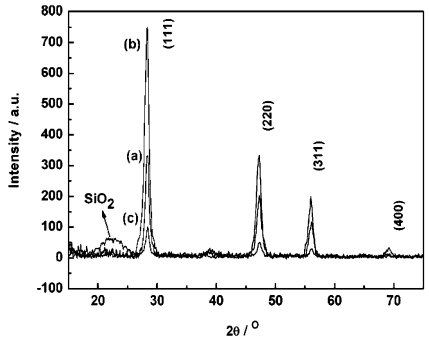

Fig. 4 XRD patterns of (a) TEOS gel heat-treated at 500 °C for 6 h, (b) the virginal Si nanoparticles, and (c) the Si/SiO nanocomposite heat-treated at 800 °C for 6 h.

After the coating, the core-shell Si/SiO nanocomposite displays better reversibility of Li insertion/extraction and higher coulombic efficiency than the virginal Si nanoparticles (see Fig. 5a). Besides, good capacity retention for the Si/SiO core-shell nanocomposite was obtained (see Fig. 5b). The SiO shell acts as a barrier to prevent the aggregation of the Si nanoparticle and serves as a buffer as well to alleviate the volume expansion during the lithiation process. Consequently, the capacity retention of the core Si nanoparticles is apparently improved. As to the decrease of the reversible capacity of Si/SiO nanocomposite compared with the virginal Si nanoparticles, this can be explained mainly by the fact that the reversible capacity of the SiO shell is lower than that of the Si nanocomposite.

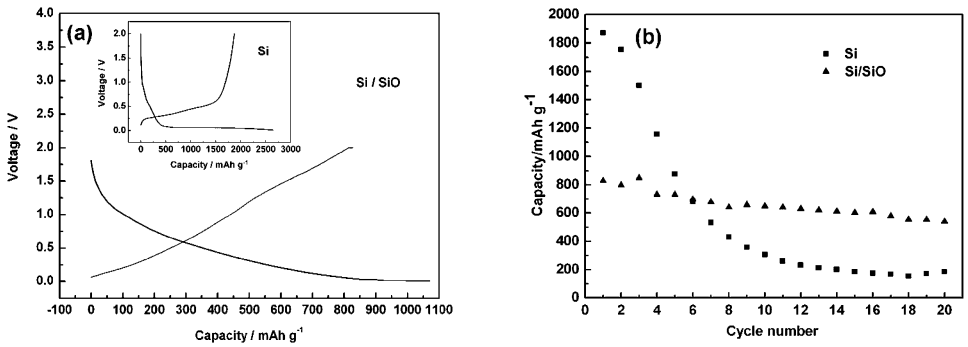

Fig. 5 (a) Charge/discharge profiles in the first cycle and (b) cycling behaviors of the Si/SiO nanocomposite and the virginal Si nanoparticles.

This research as well as the core-shell Si/C research indicates that the core-shell structure offers a promising method to improve the electrochemical performance of nano Si as electrode material for Li-ion batteries.

CORE-SHELL STRUCTURED TiO_2 NANOCOMPOSITES AND NANOPOROUS TiO_2

There is much interest in TiO_2 because of its low intercalation voltage for Li, and it can be used as electrode for rechargeable Li-ion batteries or super-capacitors [24–28]. Since nanomaterials used for anodes of Li-ion batteries show higher reversible capacity than the respective microsize materials [29–33], efforts on dispersion of nanoparticles homogeneously in a matrix [34,35] and synthesis of metal-encapsulated spherical hollow carbon [36] have been made to improve their cycling behavior. However, none

of these methods resulted in marked progress. In our group, core-shell structured TiO_2/C nanocomposites and nanoporous TiO_2 architectures were fabricated to optimize the kinetics and their electrochemical performance.

Core-shell structured TiO_2 nanocomposites

Initially a precursor, PAN-coated nano-TiO_2 particles, was formed by emulsion polymerization [12]. This precursor was heat-treated in an Ar atmosphere to achieve the core-shell structured TiO_2 nanocomposite (Fig. 6). The conductive carbon shell envelops TiO_2 nanoparticles and suppresses the aggregation of the core nanoparticles during cycling. In addition, the kinetics of Li intercalation/de-intercalation and the consequent cycling behavior are significantly enhanced (Fig. 7).

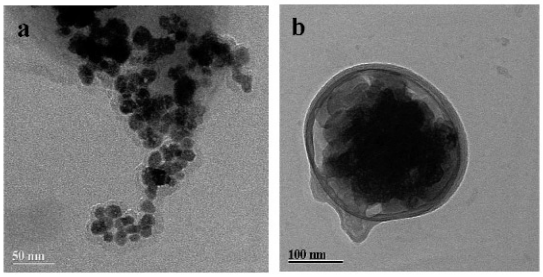

Fig. 6 TEM images of: (a) TiO_2/PAN and (b) TiO_2/C core-shell nanoparticles.

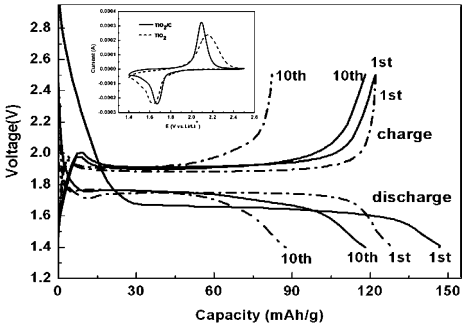

Fig. 7 Discharge and charge profiles of the virginal TiO_2 nanoparticles (dashed lines) and the TiO_2/C core-shell nanocomposites (solid lines) (at a rate of 0.25 °C) in the voltage range of 1.4–2.5 V. Inset are the CVs of TiO_2 and TiO_2/C electrodes measured at the scan rate of 0.1 mV/s.

As shown in Fig. 7, the core-shell TiO_2/C nanocomposite shows the greatly improved capacity retention. After 10 cycles, the charge capacity still remains at 96.7 % (i.e., 118 mAh/g titania) of its original capacity (i.e., 122 mAh/g titania), which is much higher than that of the virginal TiO_2 nanoparticles. The latter retained only 67.5 % of the original capacity after 10 cycles due to the nanoparticle agglomeration during the Li intercalation and de-intercalation. In addition, the kinetics and the reversibility of the nanocomposite were promoted after coating with the carbon shell, which is clearly seen from the decreased separation between reduction and oxidation peaks (ΔU) and the increased peak current in the CVs in the inset of Fig. 7. This method provides a good way to improve the cycling of nano-anode materials.

Nanoporous TiO_2

There has always been a need for development of highly porous materials with large surface area readily accessible to electrolytes, which, as a result, reduce the transport length for both electrons and ions and improve the rate capability (i.e., the power density of Li-ion batteries) [1,2]. A mesoporous TiO_2 prepared from a $TiO_2/CdSO_4$ composite intermediate was recently reported [37]. The hierarchically mesoporous TiO_2 submicron spheres with high porosity were obtained after removing the $CdSO_4$ component from the composite precursor by washing with acid solution. The reported nanosized building blocks result in excellent Li insertion/extraction performance. However, the pores on the porous sphere were distributed irregularly with the pore size varying from 3 to 50 nm according to the randomly located $CdSO_4$ component. Thus, the formation of pores not involved in charging is unavoidable.

We recently reported for the first time a strategy to prepared 3D ordered mesoporous materials, taking titania as an example [13]. Three-dimensional mesoporous microparticles of anatase titania were prepared by adopting polystyrene (PS) colloidal microparticles as a template followed by calcination in atmospheric air to remove the PS template. The preparation process of the 3D mesoporous titania is schematically shown in Scheme 1. As shown in Fig. 8, the cross-section of the prepared 3D mesoporous TiO_2 has a fcc structure, with a distance between centers of adjacent pores of about 120 nm, as a result of the replication of the PS template structure. The Brunauer–Emmett–Teller (BET) surface area of the prepared sample is 25.5 m^2/g, which is almost equal to the estimated value of 21.4 m^2/g for a 200-nm hexagonal closely packed pore.

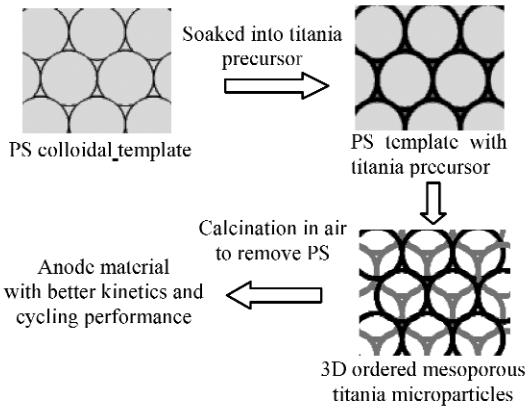

Scheme 1 Preparation process of the 3D ordered mesoporous titania microparticles formed by adopting colloidal PS crystals as a template.

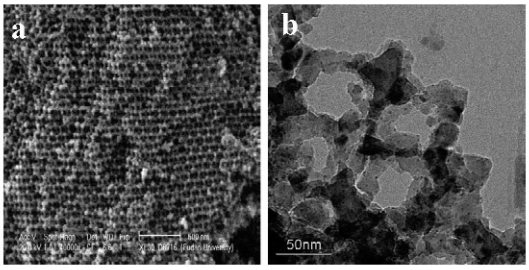

Fig. 8 (a) SEM and (b) TEM images of the synthesized 3D ordered mesoporous titania microparticles.

The CV of the 3D ordered mesoporous titania electrode is shown in Fig. 9. Based on the CV data at different scan rates, and eq. 1, the calculated apparent diffusion coefficient for the 3D ordered mesoporous titania electrode is 3.5×10^{-9} cm^2/s, which is comparable with that of the virginal nanometer titania mentioned in the above Section "Core-shell structured TiO_2 composites", 1.97×10^{-9} cm^2/s [12]. This effect is similar to that of Si/C nanocomposite [10]. The high diffusion coefficient of Li ions in the electrode can be attributed mainly to its 3D ordered mesoporous structure. The cycling performance shown in Fig. 10 represents better capacity retention at each rate compared with the reported mesoporous anatase titania [38].

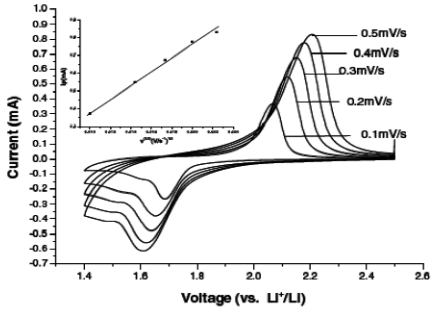

Fig. 9 CVs of the 3D ordered mesoporous TiO_2 electrode measured between 1.4 and 2.5 V vs. Li^+/Li at the scan rates of 0.1, 0.2, 0.3, 0.4, and 0.5 mV/s, respectively. The inserted figure shows that the cathodic peak currents of the CVs are in proportion to the square root of the scan rate, $v^{1/2}$.

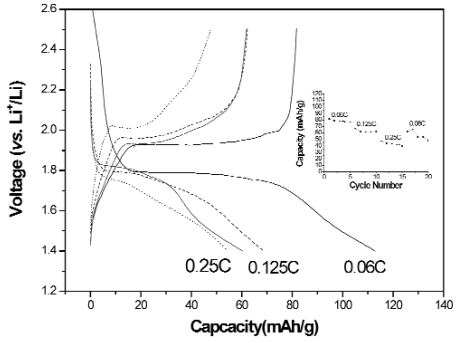

Fig. 10 The first discharge and charge curves of the 3D ordered mesoporous TiO_2 electrode in 1 mol/l $LiPF_6$ solution of DEC/EC/DMC (1:1:1, v/v/v) at different charge and discharge rates. The cycling performance of the 3D ordered mesoporous titania electrode at each rate is shown in the inserted figure.

The PS template particle size was adjusted to 250 nm to get optimized electrochemical performance of this 3D ordered mesoporous titania (Fig. 11a). Figure 11b shows that the reversible capacity and capacity retention are both promoted.

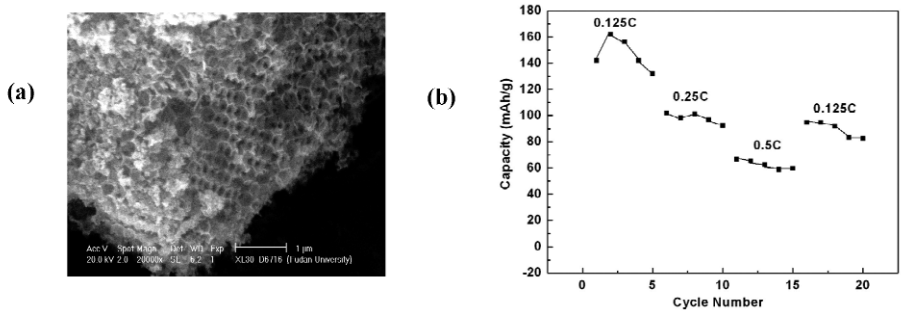

Fig. 11 (a) SEM image of the 3D mesoporous titania with an average pore size of 250-nm diameter; (b) corresponding cycling performance of the optimized mesoporous titania electrode at rates of 0.125, 0.25, and 0.5 C.

NOVEL MoO_2 NANO-ANODE MATERIAL

Molybdenum dioxide exhibits higher capacity than commercial carbonaceous materials as an anode material for Li-ion batteries [39]. We described the first synthesis of tremella-like MoO_2 consisting of nanosheets by a hydrothermal method involving the reduction of MoO_3 to MoO_2 by an ethylenediamine (EDA) reducer and an Fe_2O_3 assisting agent [13]. The prepared product presents a tremella-like structure consisting of ultrathin nanosheets with a thickness less than 10 nm (Fig. 12a). The selected area electron diffraction (SAED) pattern (inset of Fig. 12a) clearly confirms the hexagonal MoO_2 polycrystalline structure (JCPDS: 50-0739). Furthermore, the transmission electron microscopy (TEM) image at high magnification (Fig. 12d) exhibits a novel layered structure with the interplanar spacing of 1.1 nm from the side view of the nanosheets, which does not correspond to any interplanar crystal spacing of the typical MoO_2 crystal. This structure is probably due to the intercalation of excessive EDA molecules in the reaction system, which can be confirmed by the appearance of stretching vibra-

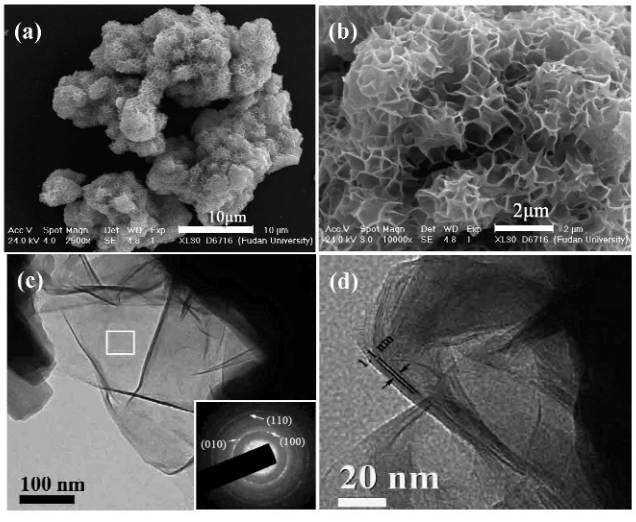

Fig. 12 SEM (a, b) and TEM (c, d) images of the as-prepared tremella-like MoO_2 at different magnifications. The SAED pattern (inset of c) was obtained on the nanosheet (marked by the frame) shown in (c), indicating the typical MoO_2 polycrystalline structure. The interplanar spacing of 1.1 nm of this novel layerered structure is identified in (c).

tion bands of $–CH_2–$ (3255, 3187 cm^{-1}), $–NH_2$ (2921, 2847 cm^{-1}), and C–N (1027 cm^{-1}) in the Fourier transform–infrared (FT–IR) spectrum of the product [14]. Energy-dispersive X-ray (EDX) and X-ray photoelectron spectroscopy (XPS) analyses show that little Fe residue was observed in the surface composition of the product.

As a result, the material shows high reversible capacity and good cycling performance even at a current density as high as 5.0 mA/cm^2 (Figs. 13a and 13b). The electrodes deliver high reversible capacities of 538.0, 314.6, and 259.4 mAh/g at current densities of 0.5, 2.5, and 5.0 mA/cm^2, respectively. In subsequent cycles, the reversible capacities increase up to around 650, 400, and 350 mAh/g, respectively. This increase is probably due to the ultra-thin nanosheet layers becoming saturated with the electrolyte upon discharge and charge after several cycles, and additionally an activation process may be obtained. In Fig. 13a, apart from the irreversible cathodic discharge capacity which may relate to the reduction of solution species to form a passivating surface film on the anode (see the small peak at about 0.6 V), there are two redox couples at 1.8/2.0 and 0.75/1.46 V, respectively, corresponding to the phase transitions in the partially lithiated Li_xMoO_2 [40]. There is no peak for the redox behavior of Fe_2O_3 and its reduced compounds in the CV curves, probably because the amount of Fe_2O_3 is small and rests in the center of the tremella body. This novel MoO_2 material shows potential application as anode material for Li-ion batteries.

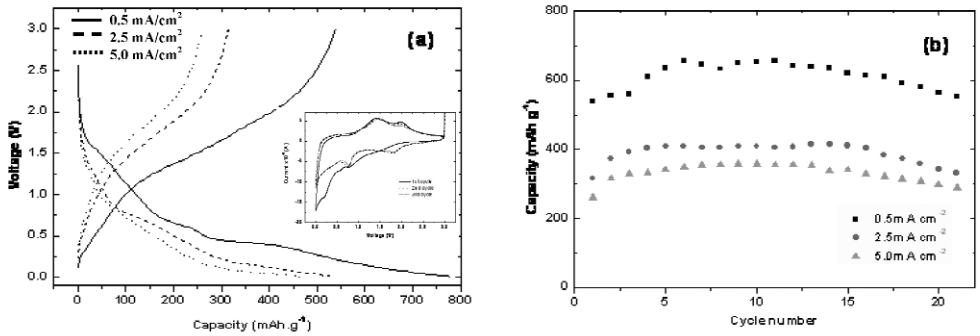

Fig. 13 (a) Discharge and charge curves for the initial cycle and (b) cycling performance of the tremella-like MoO_2 in the range of 0.01–3 V vs. Li metal at the current density of 0.5, 2.5, and 5.0 mA/cm^2, respectively. The inset in (a) shows the CVs for the as-prepared MoO_2 in the range of 0–3 V vs. Li metal at the scan rate of 0.05 mV/s.

ONE-DIMENSIONAL SnO_2 MATERIALS COATED WITH IN SITU FORMED AMORPHOUS CARBON NANOTUBES

Conventional Li-storage materials suffer serious capacity loss when they are charged or discharged at a high rate. Polarization caused by slow diffusion of Li ions and electrons in active materials is one of the challenging problems. To solve this problem, preparation of ultra-fine electrode materials [41,42] and architectures with dimensional confinement, such as nanotube (NT) or NW structures, have been tried [43,44]. Here we demonstrate some of the latest progress in SnO_2 materials coated with in situ formed amorphous carbon nanotubes (a-CNTs) in our laboratory.

One-dimensional SnO_2 materials were recently reported to be fabricated by thermal evaporation [45–50], the solution precursor route [51], and the template method [52,53]. Up to now, synthesis of single-crystal SnO_2 NWs has mainly involved vapor transport processes, and the resulting NWs are entangled. However, thermal evaporation requires high temperatures (1000–1350 °C) [45–50]. Other methods mainly result in polycrystalline array structures [52].

We report on the development of an easy fabrication method for highly ordered tetragonal single-crystal SnO_2 NW arrays using AAO (anodic alumina oxide) membrane as a template via a sol-gel route.

A typical scanning electron microscopy (SEM) micrograph of the AAO membrane is shown in Fig. 14. a-CNT-coated single-crystal SnO_2 NWs with a mean diameter of ca. 80 nm were synthesized by annealing the anodic alumina membrane in air filled with a SnO_2 sol made from $SnCl_2{\cdot}2H_2O$ and citric acid [15].

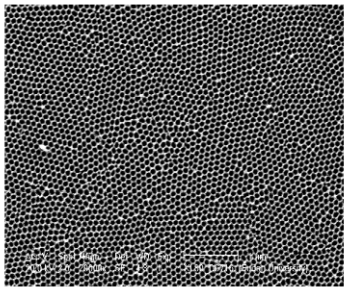

Fig. 14 SEM image of AAO.

Uniform SnO_2 NWs were observed after the alumina was partially (Fig. 15a) and totally (Fig. 15b) removed by the alkali solution. The typical high-resolution TEM micrograph (Fig. 15d) of the single SnO_2 NW (Fig. 15c) shows the single-crystal structure. The interplanar spacing of the marked (110) facets was measured to be 0.332 nm. Analysis of the SAED pattern reveals that the tetragonal SnO_2 crystal structure is consistent with the rutile SnO_2 (P42/*mnm*, JCPDS No. 41-1445).

A carbon layer with an average thickness of about 7 nm was observed on the surface of the SnO_2 NWs, indicated with a black arrow (Figs. 15c and 15d). The outer carbon layer can be removed after further annealing the template-free SnO_2 NWs in air at 450 °C for 1 h, while the color transformation from black to pure white can be obviously observed.

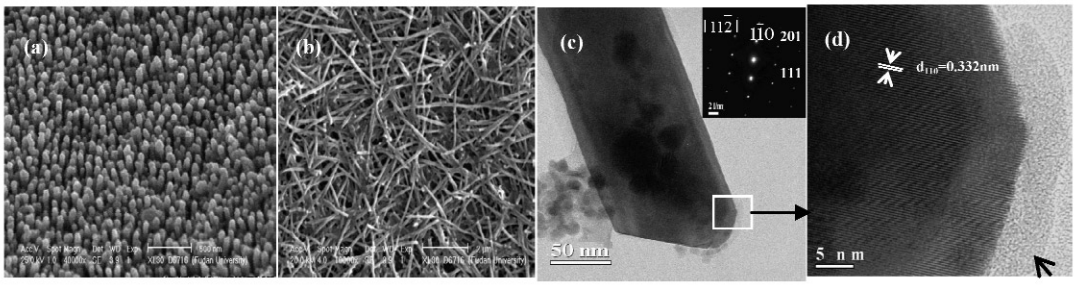

Fig. 15 SEM images of SnO_2 NWs after the AAO template was (a) partially and (b) totally removed by immersing in 0.5 and 1 M NaOH solution for 2 and 4, respectively; (c) TEM image of single SnO_2 wire; the inset is the SAED pattern of the single-crystal SnO_2 NW in picture (c); (d) HRTEM micrograph of the area marked in picture (c) with a square. The black arrow indicates the in situ formed thin layer.

When the concentration of the SnO_2 sol is decreased, CNT-coated polycrystalline SnO_2 NWs can be synthesized. As seen in Figs. 16a and 16b, the NWs are composed of many nanoparticles which are situated in the walls of the CNTs with a mean diameter of 70 nm (according to the reproduced AAO nanopores). It seems that the crystallization process was weakened since the interconnection between the nuclei was lessened when the SnO_2 precursor was applied. As a result, the scattered nanoparticles were unable to grow into one single crystal in the calcination process. The SAED pattern in Fig. 16c confirms the polycrystalline SnO_2 microstructure.

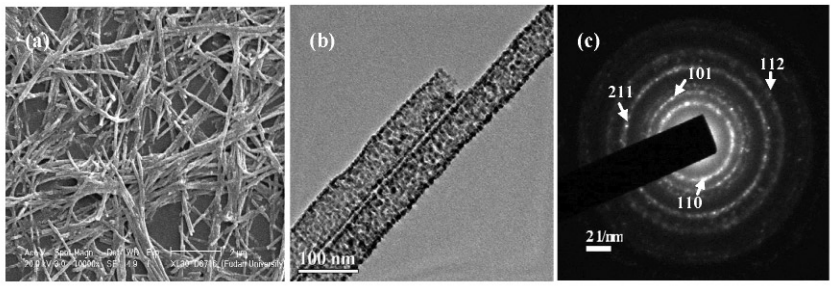

Fig. 16 (a) SEM and (b) TEM images of polycrystalline SnO_2 NWs after the AAO template was totally removed by immersing in 1 M NaOH solution for 4, and (c) the corresponding SAED pattern of the polycrystalline SnO_2 NWs.

The galvanostatic charging and discharging curves in Fig. 17 are in agreement with the normal slopes of powder SnO_2, and there is no great difference between single-crystal and polycrystalline SnO_2 NWs. The polarization of the single-crystal NWs generally seems to be larger than that of the polycrystalline NWs during the charging and discharging processes, and the reversible capacity of the single-crystal NWs is a little less than that of the polycrystalline NWs. It is clear that the interstices in the polycrystalline SnO_2 NWs allow liquid electrolyte to penetrate into the tube so that the inside SnO_2 material is easily activated, while the activation process of the single-crystal SnO_2 NWs is not fast because the tubes are relatively full.

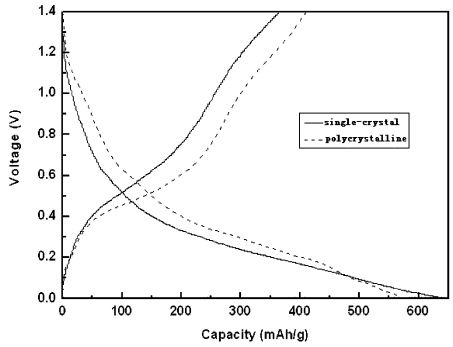

Fig. 17 Galvanostatic charge and discharge curves of the single-crystal NWs and polycrystalline NWs in the 2nd cycle.

NW arrays of a-CNT-coated single-crystal and polycrystalline SnO_2 NWs can be easily fabricated by this method. They show great promise for application as anodes in Li-ion batteries for use in nanodevice power supply. In addition, other NW arrays of a-CNTs coated oxides can also be prepared by this process.

CONCLUSIONS

Anode materials with nanostructured architectures recently studied in our laboratory include core-shell structured Si nanocomposites, TiO_2 nanocomposites, MoO_2 material, and a-CNT-coated SnO_2 NWs. These results show that the size effect, dimensional confinement, and the congruence of the carrier screening length of these elaborate nanocomposites generally lead to higher reversible capacity, better cycling behavior, and high-rate capability than their simpler antecedents. Other nanosized composites

are also of great promise for application [54–57]. It is expected that nanomaterials will greatly promote the development of Li-ion batteries.

ACKNOWLEDGMENTS

Valuable suggestions from Prof. D. Y. Zhao and associate Prof. B. D. Yao, supply of monodisperse PS microspheres from Dr. Y. H. Deng in Fudan University, and financial support from the National Basic Research Program of China (973 Program No. 2007CB209702) and the Natural Science Foundation Committee (50573012) are greatly appreciated.

REFERENCES

1. J. Maier. *Nat. Mater.* **4**, 805 (2005).
2. A. S. Arico, P. G. Bruce, B. Scrosati, J. M. Tarascon, W. V. Schalkwijk. *Nat. Mater.* **4**, 366 (2005).
3. J. Maier. *Faraday Discuss.* **134**, 51 (2007).
4. Y. F. Zhukovskii, P. Balaya, E. A. Kotomin, J. Maier. *Phys. Rev. Lett.* **96**, 58302 (2006).
5. N. Li, C. R. Martin, B. Scrosati. *Electrochem. Solid State Lett.* **3**, 316 (2000).
6. N. Li, C. R. Martin. *J. Electrochem. Soc.* **148**, A164 (2001).
7. M. Winter, J. O. Besenhard. *Electrochim. Acta* **45**, 31 (1999).
8. T. Moritaz, N. Takami. *J. Electrochem. Soc.* **153**, A425 (2006).
9. F. Jiao, K. M. Shaju, P. G. Bruce. *Angew. Chem., Int. Ed.* **44**, 6550 (2005).
10. T. Zhang, L. J. Fu, J. Gao, L. C. Yang, Y. P. Wu, H. Q. Wu. *Pure Appl. Chem.* **78**, 1889 (2006).
11. T. Zhang, J. Gao, H. P. Zhang, L. C. Yang, Y. P. Wu, H. Q. Wu. *Electrochem. Commun.* **9**, 886 (2007).
12. L. J. Fu, H. Liu, H. P. Zhang, C. Li, T. Zhang, Y. P. Wu, R. Holze, H. Q. Wu. *Electrochem. Commun.* **8**, 1 (2006).
13. L. J. Fu, T. Zhang, Q. Cao, H. P. Zhang, Y. P. Wu. *Electrochem. Commun.* **9**, 2140 (2007).
14. L. C. Yang, Q. S. Gao, Y. H. Zhang, Y. Tang, Y. P. Wu. *Electrochem. Commun.* **10**, 118 (2008).
15. N. H. Zhao, G. J. Wang, Y. Huang, B. Wang, B. D. Yao, Y. P. Wu. *Chem. Mater.* **20**, 2612 (2008).
16. Y. P. Wu, X. B. Dai, J. Q. Ma, Y. J. Chen. *Lithium Ion Batteries—Practice and Applications*, Chemical Industry Press, Beijing (2004).
17. J. O. Bensenhard, J. Yang, M. Winter. *J. Power Sources* **68**, 87 (1997).
18. H. Li, X. Huang, L. Chen. *Solid State Ionics* **135**, 181 (2000).
19. T. Moritaz, N. Takami. *J. Electrochem. Soc.* **153**, A425 (2006).
20. Y. Zhang, Z. W. Fu, Q. Z. Qin. *Electrochem. Commun.* **6**, 484 (2004).
21. Y. Liu, K. Hanai, T. Matsumura, N. Imanishi, A. Hirano, Y. Takeda. *Electrochem. Solid State Lett.* **7**, A492 (2004).
22. S. Hwang, H. Lee, S. Jang, S. Lee, H. Baik, J. Lee. *Electrochem. Solid State Lett.* **4**, A97 (2001).
23. J. R. Dahn, J. W. Jiang, L. M. Moshurchak, M. D. Fleischauer, C. Buhrmester, L. J. Krause. *J. Electrochem. Soc*. **152**, A1283 (2005).
24. P. Wang, S. M. Zakeeruddin, J. E. Moser, M. K. Nazeeruddin, T. Sekiguchi, M. Gratzel. *Nat. Mater.* **2**, 402 (2003).
25. A. Hagfeldt, M. Grätzel. *Chem. Rev.* **95**, 49 (1995).
26. Z.-R. Tian, W. Tong, J.-Y. Wang, N.-G. Duan, V. V. Krishnan, S. L. Suib. *Science* **276**, 926 (1997).
27. Y. C. Yeh, T. T. Tseng, D. A. Chang. *J. Am. Ceram. Soc.* **73**, 1992 (1990).
28. Y. K. Zhou, L. Cao, F. B. Zhang, B. L. He, H. L. Li. *J. Electrochem. Soc.* **150**, A1246 (2003).
29. A. H. Whitehead, J. M. Elliott, J. R. Owen. *J. Power Sources* **33**, 81 (1999).
30. J. Yang, Y. Takeda, N. Imanishi, O. Yamamoto. *J. Electrochem. Soc.* **146**, 4009 (1999).
31. J. Yang, Y. Takeda, N. Imanishi, T. Ichikawa, O. Yamamoto. *J. Power Sources* **79**, 220 (1999).
32. N. Li, C. R. Martin, B. Scrosati. *Electrochem. Solid State Lett.* **3**, 316 (2000).

33. N. Li, C. R. Martin. *J. Electrochem. Soc.* **148**, A164 (2001).
34. I. Kim, P. N. Kumta, G. E. Blomgren. *Electrochem. Solid State Lett.* **3**, 493 (2000).
35. S. Hwang, H. Lee, S. Jang, S. M. Lee, S. J. Lee, H. Baik, J. Lee. *Electrochem. Solid State Lett.* **4**, A97 (2001).
36. K. T. Lee, Y. S. Jung, S. M. Oh. *J. Am. Chem. Soc.* **125**, 5652 (2003).
37. Y. G. Guo, Y. S. Hu, J. Maier. *Chem. Commun.* **26**, 2783 (2006).
38. B. Zhang, Y. Yuan, Y. Wang, Z. W. Fu. *Electrochem. Solid State Lett*. **9**, A101 (2006).
39. J. J. Auborn, Y. L. Barberio. *J. Electrochem. Soc*. **134**, 638 (1987).
40. Y. Liang, S. Yang, Z. Yi, J. Sun, Y. Zhou. *Mater. Chem. Phys.* **93**, 395 (2005).
41. F. Jiao, K. M. Shaju, P. G. Bruce. *Angew. Chem., Int. Ed*. **44**, 6550 (2005).
42. H. Liu, L. J. Fu, H. P. Zhang, J. Gao, C. Li, Y. P. Wu, H. Q. Wu. *Electrochem. Solid State Lett.* **9**, A529 (2006).
43. C. N. R. Rao, M. Nath. *Dalton Trans.* **1**, 1 (2003).
44. B. Patzke, F. Krumeich, R. Nesper. *Angew. Chem., Int. Ed.* **41**, 2446 (2002).
45. W. Yu, X. Li, X. Gao, F. Wu. *J. Phys. Chem. B* **109**, 17078 (2005).
46. J. Hu, X. Ma, N. Shang, Z. Xie, N. Wong, C. Lee, S. Lee. *J. Phys. Chem. B* **106**, 3823 (2002).
47. Z. Pan, Z. Dai, L. Wang. *Science* **291**, 1947 (2001).
48. Z. Dai, J. Gole, J. Stout, Z. Wang. *J. Phys. Chem. B* **106**, 1274 (2002).
49. R. Zhang, Y. Lifshitz, S. Lee. *Adv. Mater.* **15**, 635 (2003).
50. N. Ramgir, I. Mulla, K. Vijayamohanan. *J. Phy. Chem. B* **108**, 14815 (2004).
51. Y. Wang, X. Jiang, Y. Xia. *J. Am. Chem. Soc.* **125**, 16176 (2003).
52. M. Zheng, G. Li, X. Zhang, S. Huang, Y. Lei, L. Zhang. *Chem. Mater.* **13**, 3859 (2001).
53. H. Cao, X. Qiu, Y. Liang, L. Zhang, M. Zhao, Q. Zhu. *ChemPhysChem* **7**, 497 (2006).
54. L. C. Yang, Q. S. Gao, Y. Tang, Y. P. Wu, R. Holze. *J. Power Sources* **179**, 357 (2008).
55. L. J. Fu, H. P. Zhang, Q. Cao, G. J. Wang, L. C. Yang, Y. P. Wu. *Microporous Mesoporous Mater*. (2008). Accepted for publication.
56. W.-Y. Li, L.-N. Xu, J. Chen. *Adv. Funct. Mater.* **15**, 851 (2005).
57. H. K. Liu, G. X. Wang, Z. Guo, J. Wang, K. Konstantinov. *J. Nanosci. Nanotechnol.* **6**, 1 (2006).